



Full Length Article

Defects or charge transfer: Different possibilities to explain the photoluminescence in crystalline $\text{Ba}(\text{Zr}_x\text{Ti}_{1-x})\text{O}_3$ 

Agda E. Souza^{a,*}, Guilherme S. Sasaki^a, Sabrina A. Camacho^a, Silvio R. Teixeira^a,
Maximo S. Li^b, Elson Longo^c

^a Universidade Estadual Paulista, Faculdade de Ciências e Tecnologia, Presidente Prudente, SP, Brazil

^b Universidade de São Paulo, Instituto de Física, São Carlos, SP, Brazil

^c Universidade estadual Paulista, Instituto de Química, Araraquara, SP, Brazil

ARTICLE INFO

Article history:

Received 15 January 2016

Received in revised form

16 May 2016

Accepted 14 June 2016

Available online 21 June 2016

Keywords:

BZT

Photoluminescence

Defects

Charge transfer

ABSTRACT

In this work, BZT ($\text{Ba}(\text{Zr}_x\text{Ti}_{1-x})\text{O}_3$), composite ceramic powder with $x=0, 0.25, 0.50, 0.75$ and 1 (mol) was prepared by the microwave-assisted hydrothermal method. The structural, morphological and optical properties of the compounds were determined by XRD, SEM, Raman, UV–vis and photoluminescence analysis. The results showed that the stability of the BZ phase was strongly influenced by the isomorphous Zr/Ti substitution, and that the BZ sample had the greatest structural order for short and long distances compared to the other. The BZT ceramic composite showed optical behavior also influenced by the concentration of Zr, resulting in a growing photoluminescence emission with increasing Zr ion in the network. The BZ sample showed higher photoluminescent intensity in a region including the entire visible spectrum. Although the effect of photoluminescence in these materials is dependent on the presence of defects, which produce excitons for radiative recombination, in the BZ compound, there might have been other effects causing the intense photoluminescence. In this case, high emission is associated with the a charge transfer between neighboring clusters $[\text{ZrO}_6]$ in a nanoparticle surface interface, which in turn are joined to form BZ mesocrystals on a micrometer scale. The photoluminescence observed in the BZT compound had a predominantly white color, a feature that gives it high potential for applications in white light-emitting devices.

© 2016 Elsevier B.V. All rights reserved.

1. Introduction

BaTiO_3 ceramic material with perovskite structure has been a historical object of study carried out in an evolutionary and uninterrupted way. This interest has arisen from the possibility of wider applications of this material, because of its various properties, mainly electrical and optical [1]. In general, researchers have invested continuously in studies to improve or promote the properties of this compound, without changing its basic structure. The simplest way to achieve this goal is through controlled doping or replacement of its cations. Thus, there are many other compounds such as $\text{Ba}(\text{Zr}/\text{Ti})\text{O}_3$ or BZT. The literature reports that BZT with perovskite structure is formed by a complete solid solution of ferroelectric BaTiO_3 (BT) with the paraelectric BaZrO_3 (BZ) [2]. BZ shows photoluminescence properties at room temperature [3,4] and has a high melting temperature, which gives it good mechanical strength, high thermal and chemical stability and low

thermal expansion coefficient. These features allow BZ to have applications in the manufacture of inert crucibles and substrates for high temperatures, and even in the aerospace industry [5]. The BZT solid solution formed by BT and ZT compounds, within a limit of Ti/Zr substitution, may have new properties or improve those existing in separate phases. The interest and attention focused on BZT are due to its potential applications involving piezoelectric transducers, DRAM, microwave devices and energy storage, among many others. Recently, BZT has been chosen as an alternative material to replace $(\text{Ba}, \text{Sr})\text{TiO}_3$ in the manufacture of ceramic capacitors due to system stability. This stability is achieved with the replacement of Ba^{4+} by Zr^{4+} , which is chemically more stable [6]. Also, several methods have been reported for the preparation of the BZT compound, including solid state reaction, sol-gel, self-combustion, co-precipitation and hydrothermal techniques [2,7–11]. The use of different synthesis methods associated with different precursors in the production of ceramic compounds, such as BZT, may result in different architectures, different particle sizes, variations in the purity of the phases, and especially different properties of the material. In this work, the controlled synthesis of BZT ceramic powder was performed using the

* Corresponding author.

E-mail address: agda@fct.unesp.br (A.E. Souza).

microwave-assisted hydrothermal method under low-temperature conditions and reducing the processing time. The structural and morphological characteristics of the BZT compound were evaluated. The optical property of photoluminescent emission at room temperature was investigated and discussed according to structural arrangement and particle size.

2. Materials and methods

BZT was prepared using 0.01 mol $\text{BaCl}_2 \cdot 6\text{H}_2\text{O}$ (99% purity), $\text{ZrOCl}_2 \cdot 8\text{H}_2\text{O}$ (99.9%, Alfa Aesar) and $\text{C}_{12}\text{H}_{28}\text{TiO}_4$ (97%, Aldrich) as precursors, and NaOH (97%, 15 mol/l), as mineralizer. The x concentration of the $\text{Ba}(\text{Zr}_{1-x}\text{Ti}_x)\text{O}_3$ compound varied, where it was 0, 0.25, 0.50, 0.75 or 1 (mol). The chloride precursors, at appropriate amounts, were added to a beaker containing approximately 30 ml of deionized water. Subsequently, an adjusted concentration of titanium isopropoxide was added to the solution, followed by rapid addition of 50 ml of mineralizer. Throughout this process, the solution was subjected to ultrasound for approximately 10 min. Afterwards, the solution was transferred to a Teflon[®] collection cup, with a total capacity of 110 ml and placed inside a hermetically sealed reaction cell, which was placed in a household domestic microwave oven with 2.45 GHz radiation and maximum power of 800 W, fashioned with a time and temperature controller. The ceramic powder was synthesized at a heating rate of 140 °C/min and maintained at 140 °C for 80 min, reaching a maximum pressure of 7 kgf/cm² (~7 bar). At the end of the reaction time, the system was allowed to cool to room temperature, washed with deionized water to neutral pH (pH~7) and then dried in an oven at 110 °C for 12 h. The BZT ceramic powder was characterized by X-ray diffraction (XRD) using a Shimadzu XRD-6000 model, Cu $\text{K}\alpha_1$ ($\lambda=1.5406$ Å) and Cu $\text{K}\alpha_2$ ($\lambda=1.5444$ Å), tension of 40 kV and 30 mA. The scan was done in a range of 2θ angles of 10° to 80°, using divergence and reception slits of 1° in continuous scan mode, with 0.02° steps and scanning speed of 2°/min. Characterization by Raman spectroscopy was also performed using a micro-Raman spectrograph, a Renishaw inVia model equipped with a Leica microscope (50× objective, spatial resolution of 1 μm^2) and a CCD detector. Spectra were scanned between 100 and 1400 cm^{-1} , with five accumulations, using a He–Ne laser with a 633 nm wavelength. UV–visible absorbance (UV–vis) characterization was done by diffuse reflectance, using a Cary 5G Varian (UV–vis – NIR) spectrophotometer in total reflection mode. The equipment was calibrated with two Labsphere reflectance standards, SRS 94-010 (white, 99% reflection) and SRD 02-010 (black, 0.2% reflection). The region analyzed was 800 to 200 nm with a 600 nm/min step and an exchange lamp (Visible–Ultraviolet) at 350 nm. UV–vis absorbance measurements were used to determine the optical band gap of each sample by the Wood and Tauc method [12]. Photoluminescence spectra of BZT samples were obtained using a Thermal Jarrel-Ash Monoscope 27 with a Hamatsu R446 photomultiplier coupled to an acquisition system composed of a lock-in SR-530. The excitation energy corresponds to a krypton ion laser (Coherent Innova) with a wavelength of 350.7 nm and output power of 200 mW. The samples were used as a powder and measurements were performed at room temperature. The ceramic powder morphology was observed using field emission scanning electron microscopy images (FE–SEM). For this, we used Zeiss equipment, Supra[™] 35 model, equipped with an in-lens detector for better and higher resolution.

3. Results

The X-rays diffraction patterns of the BZT compound and its morphology are shown in Fig. 1. For the sample with $x=0$

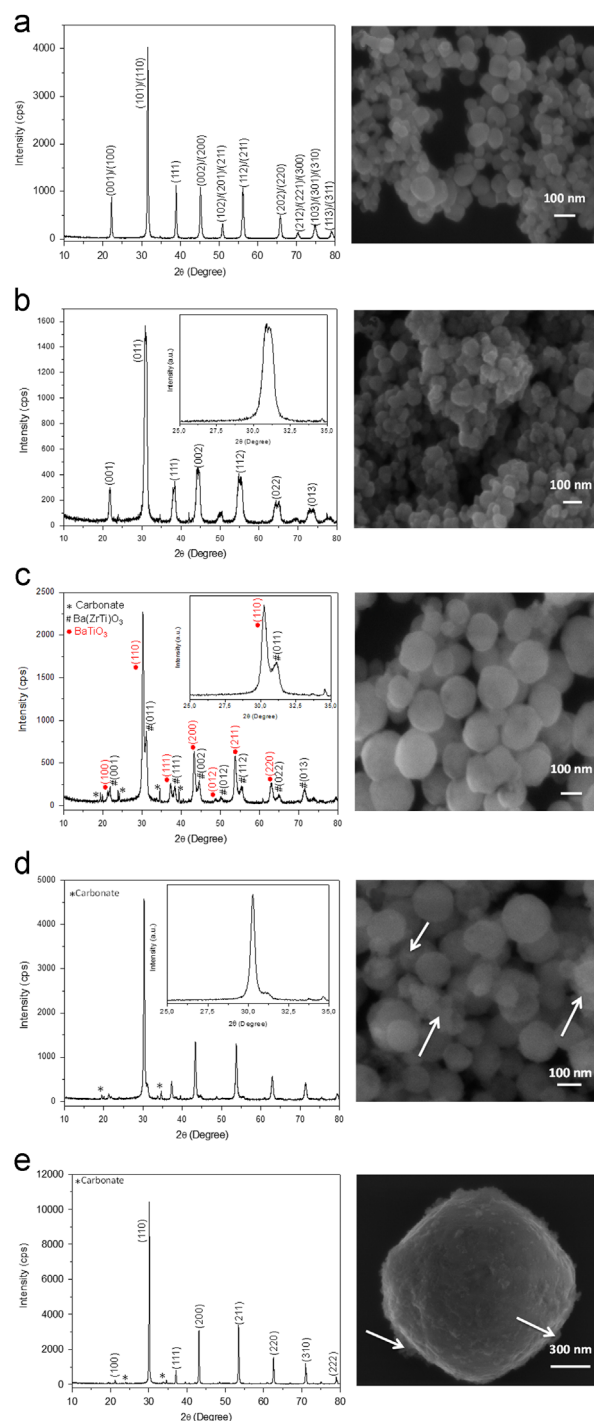


Fig. 1. XRD patterns of the $\text{Ba}(\text{Zr}_x\text{Ti}_{1-x})\text{O}_3$ samples: (a) $x=0$; (b) $x=0.25$; (c) $x=0.50$; (d) $x=0.75$; (e) $x=1$.

(Fig. 1(a)), a tetragonal phase BaTiO_3 (JPCDS 79-2264) was observed. This tetragonality is discussed in terms of the diffraction peak around $2\theta=45^\circ$. In this case, the peak corresponding to the (200) cubic phase transforms into a doublet correlating with the (200) and (002) planes of tetragonal BaTiO_3 . However, the observation of this duplicity in the XRD pattern of this sample was not as evident, because the difference between the lattice parameters of BaTiO_3 tetragonal phase was quite small. This tetragonal symmetry, however, could be confirmed by Raman spectroscopy data, which will be discussed later. The scanning electron microscopy image (FE–SEM) of this sample ($x=0$ – BaTiO_3) showed that growth generates nanostructures close to having spherical

morphology, whose particle size did not exceed 100 nm. In previous studies [13,14], the growth of BaTiO₃ spherical particles prepared under similar conditions using 6 mol/L KOH as mineralizer was also observed. However, barium carbonate as additional phase was identified and the particle observed by FE-SEM images showed sizes greater than 100 nm. Note, therefore, that the mineralizer used herein (15 mol/l NaOH) contributed to the precipitation of single phase BaTiO₃, but inhibited the growth of nanoparticles.

When $x=0.25$ concentration of Zr was added to the BaTiO₃ network, the formation of a solid solution of Ba(Zr_{0.25}Ti_{0.75})O₃ (BZT25) with cubic symmetry (JPCDS 36-19) was observed, characterized by large and less intense XRD peaks (Fig. 1(b)), compared to the BaTiO₃ sample. Also, there was evidence that the solid solution of BZT25 was not completely formed, since the diffraction peaks appeared as overlapped doublets, as can be seen in the insert graph in Fig. 1(b) corresponding to the peak (001) of the BZT25 sample. It was therefore observed that the BaTiO₃ phase also occurred at the beginning of the formation of the BZT solid solution, showing incipient crystallization in the $x=0.25$ compound. Seeharaj and colleagues [2] argue that strongly alkaline conditions (≥ 15 M NaOH) favor the chemical equilibrium of the reaction during the BZT phase formation, but do not prevent the precipitation of secondary phases. Accordingly, some less intense XRD peaks were observed, which could also have corresponded to the formation of carbonates as an additional phase. For this concentration ($x=0.25$) was again observed favoring spherical particles of a few nanometers in size (FE-SEM image – Fig. 1(b)). There was no homogeneity in particle size, and the agglomerates were denser, probably due to the carbonate phase acting as a "cementing" agent between BZT25 nanoparticles.

In the sample with $x=0.50$ Zr in the BaTiO₃ network (BZT50), the formation of two main phases was identified along with traces of barium carbonate phase. One of the phases identified corresponded to the BZT solid solution, having the same diffraction pattern of the sample with $x=0.25$ (JPCDS 36-19). However, together with this solid solution, there was the formation of a BaZrO₃ cubic phase (JPCDS 74-1299), as evidenced by the most intense peaks being concomitant with those of the BZT phase (see insert Fig. 1(c)). By means of the diffraction peak profile observed (Fig. 1(c)), there was evidence that BZT solid solution formation was less favorable, because the diffraction peaks were less defined and less intense, when compared to the $x=0.25$ concentration. There were also diffraction peaks indicative of the carbonate phase. The particles formed in this sample also exhibited a spherical architecture but with a larger size than that observed in samples with $x=0$ and $x=0.25$ concentration (> 100 nm) (Fig. 1(c)). This finding provided evidence that the phases identified (BZT and BaZrO₃), although independent, formed a single particle, which may have contributed to the increase in its dimensions.

When the Zr concentration was increased to $x=0.75$ in the BaTiO₃ network, there was BZ phase formation with higher crystallinity, since the characteristic diffraction peaks were thinner and more intense (JPCDS 74-1299). There was still evidence of peaks corresponding to the BZT phase, as can be seen in the small shoulder to the left of the peak around $2\theta=30^\circ$ (insert of Fig. 1(d)). This phase was identified using the same diffraction pattern of the sample with $x=0.25$ (JPCDS 36-19), since there was no other standard in the database to identify the BZT75 phase. This result shows that excess Zr in the BaTiO₃ network favors the formation of the BZ phase and inhibits the formation of the BZT phase. For this composition, the FE-SEM image again showed the formation of particles with a spherical appearance, but with a slight decrease in size compared to the sample with $x=0.50$. This fact was evidence that both phases composed a single particle. In this sample, there

was also the presence of characteristic diffraction peaks of the barium carbonate phase, which could be visible on FE-SEM image by a spongy appearance as indicated by the arrows in the regions of Fig. 1(d).

The formation of the cubic phase of BaZrO₃ was determined in the sample with $x=1$ (Fig. 1(e)), which was highly crystalline (JPCDS 89-2486), as indicated by narrow and very intense diffraction peaks. However, there were still indications of carbonates as a secondary phase, characterized by low intensity diffraction peaks. This phase could be observed in the FE-SEM image (Fig. 1(e)) in the regions indicated by the arrow. This image also showed that BZ particles were bigger on the order of micrometers, showing a very rough surface and apparently spherical morphology with early faceting. This faceting suggested the possible formation of octahedral architecture, as seen in the work of Macario et al. [15] and Moreira et al. [16]. These authors prepared BZ particles using Ba and Zr precursors and synthesis conditions similar to those used in this study. However, both groups used 6 mol/L KOH as mineralizer, obtaining a deca-dodecahedron morphology with well-defined surfaces. This result showed that the mineralizer and alkaline conditions influenced the morphological formation of particles and could possibly change the properties displayed by the material. Also, the surface roughness observed in the particles (Fig. 1(e)) featured structures called mesocrystals consisting of primary nanoparticles that grow following a self-assembly mechanism, yielding ordered superstructure for a non-classical growth process [17–19].

Fig. 2 shows an overlay of the most intense diffraction peaks at around $2\theta=30^\circ$ for all concentrations of the BZT sample. It can be observed from the sample with $x=0$ (BT), a distinct shift of the diffraction peaks to lower angle values (2θ), characterizing the BaTiO₃ structural phase change with Zr addition, as discussed above. A variation in the intensity of the peaks was also noted. For samples with $x=0.25$ and $x=0.50$, in which the BZT phase was more evident, the corresponding peaks present were low intensity and broader when compared with the others. This suggests that these samples had a low crystallinity, i.e., a deficient long-range structural ordering, or the presence of an incomplete solid solution. In the sample with $x=1$ (BZ), the peak intensity was relatively high and its width was relatively small, indicating that this sample had a high degree of structural order in the long range, compared to the other, i.e., high crystallinity.

Raman spectroscopy was used to complement the XRD data for the BZT samples (Fig. 3). The Raman scattering with active vibrational modes of considerable relative intensity provided local symmetry information for each compound, i.e., structural ordering information at short distance. Ba(Zr_{*x*}Ti_{1–*x*})O₃ ceramic composites

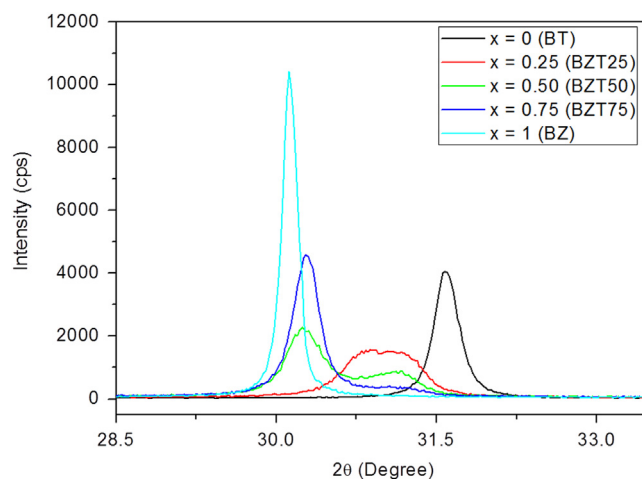


Fig. 2. XRD pattern of sample X-ray BZT around the peak of greatest intensity.

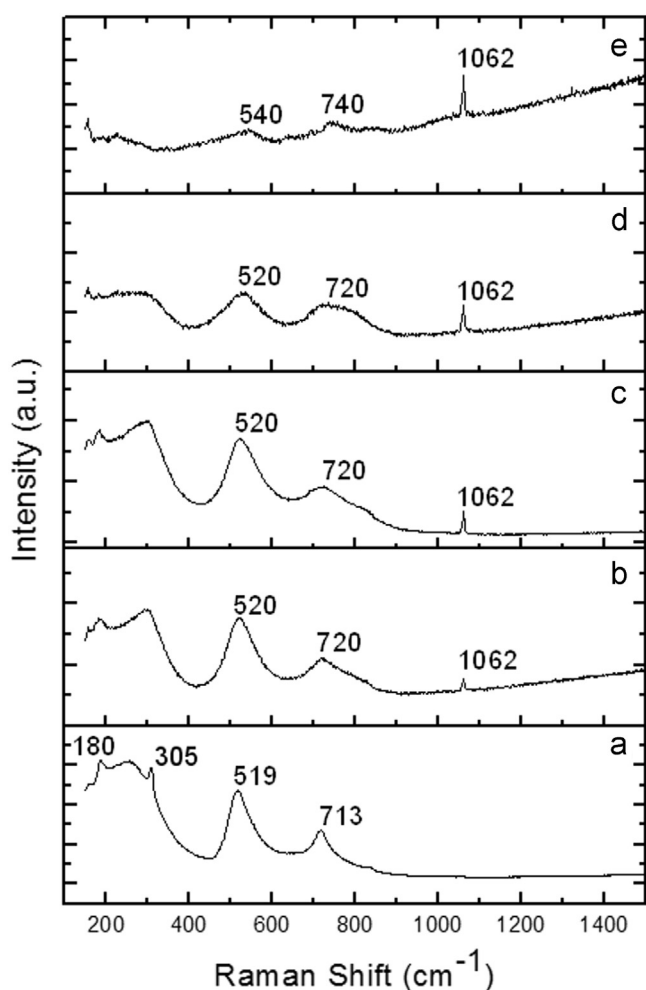


Fig. 3. Raman spectra of $\text{Ba}(\text{Zr}_x\text{Ti}_{1-x})\text{O}_3$ samples: (a) $x=0$; (b) $x=0.25$; (c) $x=0.50$; (d) $x=0.75$; (e) $x=1$.

have different symmetries depending on the stoichiometric composition and, in general, can exhibit two types of vibrational modes: longitudinal optical (LO) and transverse optical (TO), arising from vibration frequencies of network phonons of solid compounds. The BZT sample with $x=0$ (Fig. 3(a)) displayed vibrational modes that characterized the tetragonality of the BaTiO_3 phase formed. A very strong band around 180 cm^{-1} was attributed to the anharmonic coupling between three $A_1(\text{TO})$ phonons caused by impurities, stress or lattice defects. If the particles have dimensions of a few nanometers, this band will be slightly higher than the Raman shift. The intensity of the band at 305 cm^{-1} was assigned to the overlap of the $E(\text{TO}_3)+E(\text{LO}_2)+B_1$ modes [20], the band at 519 cm^{-1} corresponded to the $(\text{TO}_4)+A_1(\text{TO}_3)$ active transverse modes [21], and 713 cm^{-1} , the coupling of $E(\text{LO}_4)$ and $A_1(\text{LO}_3)$ modes, resulting in the $E(\text{LO}_4)+A_1(\text{LO}_3)$ active mode [22]. The presence of the Raman active mode at 305 cm^{-1} for the B_1 mode, indicated an asymmetry of the octahedron $[\text{TiO}_6]$ of these samples, characterizing the "fingerprint" of the BaTiO_3 tetragonal phase ($x=0$ sample) [21,22]. According to the literature, the band at 305 cm^{-1} along with the band at 713 cm^{-1} of the Raman spectrum, gives clear evidence for the tetragonality of nanometric particles in titanates, indicating that the crystal structure is, at the very least, locally tetragonal or has this symmetry at the molecular level [22,23], where these observations could not be directly confirmed by XRD measurements. With the substitution of Ti^{4+} by Zr^{4+} , it was observed that the band at 305 cm^{-1} disappeared, showing the transformation

towards a crystalline structure of cubic symmetry, as could be observed for samples with x concentrations ranging from 0.25 to 0.75 (Fig. 3(b)–(d)). The Raman modes, near 520 and 720 cm^{-1} , became slightly broader and less intense with increasing Zr concentration in the network. This was due to an increase in symmetry in the network of BZT system, for intermediate x concentrations ($x=0.25, 0.50$ and 0.75). Although the structure is cubic, these compounds have $[\text{TiO}_6]$ or $[\text{ZrO}_6]$ clusters that are distorted or show a slight inclination (tilt) without breaking of bonds, which promote the Raman active modes within the cubic matrix. In the sample with $x=1$ (BaZrO_3 , Fig. 3(e)), vibrational modes of low intensity near 540 and 740 cm^{-1} may correspond to transverse $A_1(\text{TO})$ and longitudinal $E(\text{LO})/A_1(\text{LO})$ modes, respectively. According to Charoonsuk et al. [24], BZ compounds with cubic symmetry, $Pm\bar{3}m$, have 12 optical modes represented by $3F_{1u}+F_{2u}$. These authors believe that Raman modes of the first order for cubic symmetry groups cannot be collected because all atoms in the structure occupy sites with inversion symmetry. However, these modes can become active in the cubic structure when the oxygen octahedron undergoes a slight local distortion. Defects caused by oxygen vacancies or the presence of OH^- groups, in the replacement of the oxygen atoms, are favorable conditions for these local distortions [24]. Therefore, the active modes observed in the BZ sample ($x=1$) can be associated with the asymmetry of the octahedron $[\text{ZrO}_6]$ indicating a soft spot distortion within the BaZrO_3 cubic structure. Raman modes appearing at 1062 cm^{-1} for the samples with $x \geq 0.25$ (Fig. 3(b)–(e)) corresponded to the presence of carbonates, in agreement with the XRD data.

Bundling order of identical molecules with stability of cohesive forces leads to a crystalline material. This molecular bundling results in a mutual disturbance between orbitals of a molecule and molecular orbital of its vicinity. Such perturbation implies a mixture of orbitals that are forced to rearrange energetically and distribute the total energy across the extent of the lattice, resulting in the "band structure." The band formed by bonding orbitals is called the valence band (VB), and that formed by the anti-binding orbitals, is called the conduction band (CB). The electrons located in VB have little mobility due to attraction exerted by the nuclei. However, when are taken to the CB, these electrons pass into a state of greater mobility and can move in an oriented manner in a continuous flux. In the crystalline material, VB and CB are energetically separated by a region where no electron can cross, i.e., a forbidden band, known as a band gap. This region can also be understood as the minimum energy value that the electron must receive to be elevated from VB for CB. Theoretical studies show that CB of titanates is originated by the 3d orbitals of the Ti metal, while VB is derived from the 2p orbital of oxygen. To zirconates, CB is derived from the 4d orbital of Zr [3,25]. The band gap energy can be measured by UV-Visible (UV-vis) spectroscopy. Results of this characterization, combined with the Raman spectroscopy results can provide information about local distortions of the material, caused by isomorphic substitution of ions, or cations, in the material structure. Such distortions behave as intrinsic defects resulting in some optical properties anomaly of the material. The characterization results of absorbance in the UV-vis region to the BZT samples are shown in Fig. 4. The optical band gap values (E_g) was determined by the Wood and Tauc method [12], according to Eq. (1). In this equation, h is Planck's constant, ν is the radiation frequency (UV-vis), n indicates the type of electronic transition between bands (direct transition ($n=1/2$), indirect ($n=2$), directly prohibited ($n=1/2$) and indirectly prohibited ($n=3$)) and α is a constant, or absorption coefficient, calculated by the Kubelka-Munk mathematical method [26].

$$h\nu\alpha = (h\nu - E_g)^n \quad (1)$$

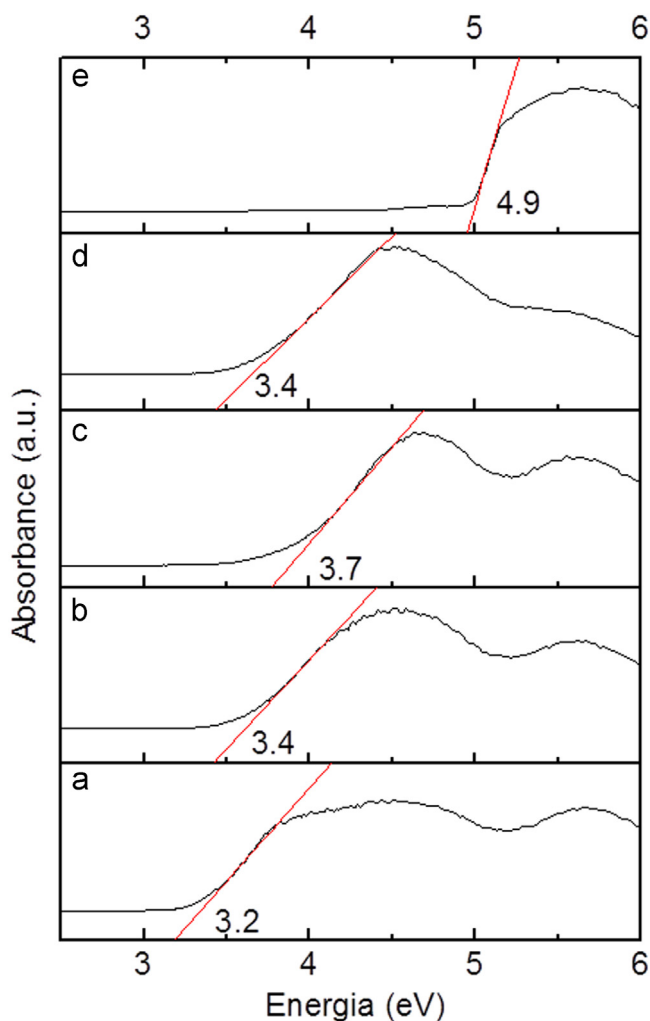


Fig. 4. UV-vis spectra in the absorbance mode \times energy of $\text{Ba}(\text{Zr}_x\text{Ti}_{1-x})\text{O}_3$ samples: (a) $x=0$; (b) $x=0.25$; (c) $x=0.50$; (d) $x=0.75$; (e) $x=1$.

In the samples with $x \leq 0.75$ (Fig. 4(a)–(d)), the gap energy showed little variation, but characteristic of a semiconductor. The behavior of the absorption curves of these samples was also similar and typical of semiconductor material. It was noted that in the lower energy region, there was a gradual tail on the absorption curve, suggesting edge or extended states near the permitted bands [12]. In other words, the behavior of the curve in this region indicated the presence of electronic states within the prohibited optical gap region, featuring intrinsic defects of these semiconductor materials. In the case of BZT samples ($x \leq 0.75$), these intermediate states could be generated due to Zr/Ti replacement, which would cause a redistribution of charge density around the atoms constituting the crystal lattice, i.e., due to movement of BV and BC involving the atoms in this region. In all cases (for all x concentrations), the presence of intermediate states allowed an indirect electron transition between VB and CB, and therefore, $n=2$ was used in Eq. (1). The behavior of the sample absorption curve with $x=1$ (BZ) indicated a material with high crystallinity or that was structurally ordered (Fig. 4(e)). The appearance of the absorption tail in the low energy region indicated the near absence of intermediate states in the band gap of this sample. This behavior could explain the increase in the gap energy value, compared to other compounds, but it was not possible to say that this compound was free of intrinsic defects. The increase in the optical gap value for the $x=1$ sample could also be explained by the increase in electronic levels of the 4d orbital of the Zr atom in the

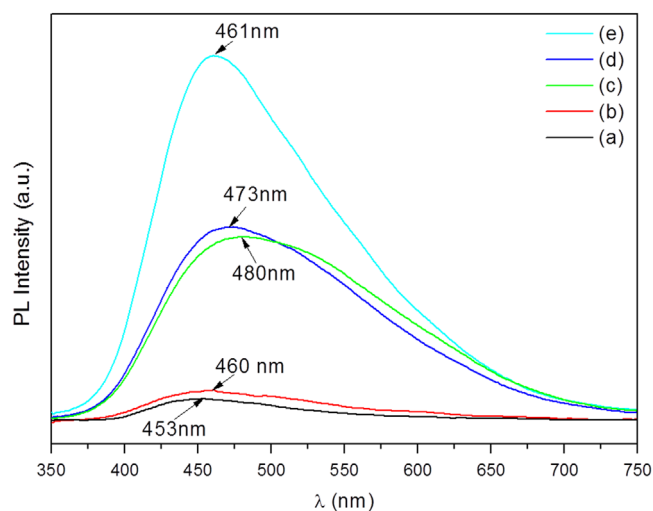


Fig. 5. Photoluminescence spectra of the $\text{Ba}(\text{Zr}_x\text{Ti}_{1-x})\text{O}_3$ samples: (a) $x=0$; (b) $x=0.25$; (c) $x=0.50$; (d) $x=0.75$; (e) $x=1$.

lattice [3]. The band gap energy value of this compound (4.9 eV) is characteristic of an insulating material, although it can also be viewed as semiconductor behavior.

The gap energy values can be used to understand the photoluminescent emission behavior in the visible spectrum region of the material. The photoluminescence property (PL) occurs when a photon of higher energy is absorbed, and a photon of lower energy is emitted. For semiconductor materials, PL in the visible range of the spectrum is explained by radiative recombination between electrons and holes trapped in the states located in the gap. The PL curve profile obtained for BZT samples, shown in Fig. 5, was typical of a multiphonon process, i.e., emissions which occur along multiple paths involving multiple states within the band gap. The intermediate states, characterized by smooth absorption edge in the low-energy UV-vis region show local structural ordering in BZT compounds (middle distance ordering). Several literature reports attribute this local structure ordering to the presence of $[\text{TiO}_6]$ or $[\text{ZrO}_6]$ clusters, while the disorder is attributed to the presence of $[\text{TiO}_5]$ and $[\text{ZrO}_5]$ clusters, distorted clusters (without bond breaking) or those containing oxygen vacancies. This local order-disorder degree is essential for the radioactive decay process to occur. The broadband shown in the PL spectra of BZT samples is characteristic of this mid-range order-disorder structure and indicates that during radioactive decay a multiphoton process occurs. In other words, there are several emissions of photons with different energies, ranging from the red to violet region of the visible spectrum, resulting in photoluminescent emission and a white color for all samples. In general, an increased PL intensity with increasing x concentration in BZT samples was observed along with a soft shift from the blue region to the green region of the spectrum, for samples with x concentration up to 0.50. This shift produces the so-called shallow and deep defects of intermediate states of the band gap. Shallow defects are associated with charge carriers trapped near the VB and CB. These shallow defects, in turn, are associated with higher energy photoluminescent emissions, i.e., emissions from blue to violet occurring in electron-hole recombination centers promoted by the defects near the VB and CB. Deep defects are associated with the entrapment of charge carriers with more distant of VB and CB and are considered the emission centers responsible for photoluminescence in the less energetic regions of the visible spectrum (green to red). In the case of $x \leq 0.50$ BZT samples, it is possible that radiative recombination occurred with carriers near its BV and BC decays, favoring the blue region of the spectrum, according

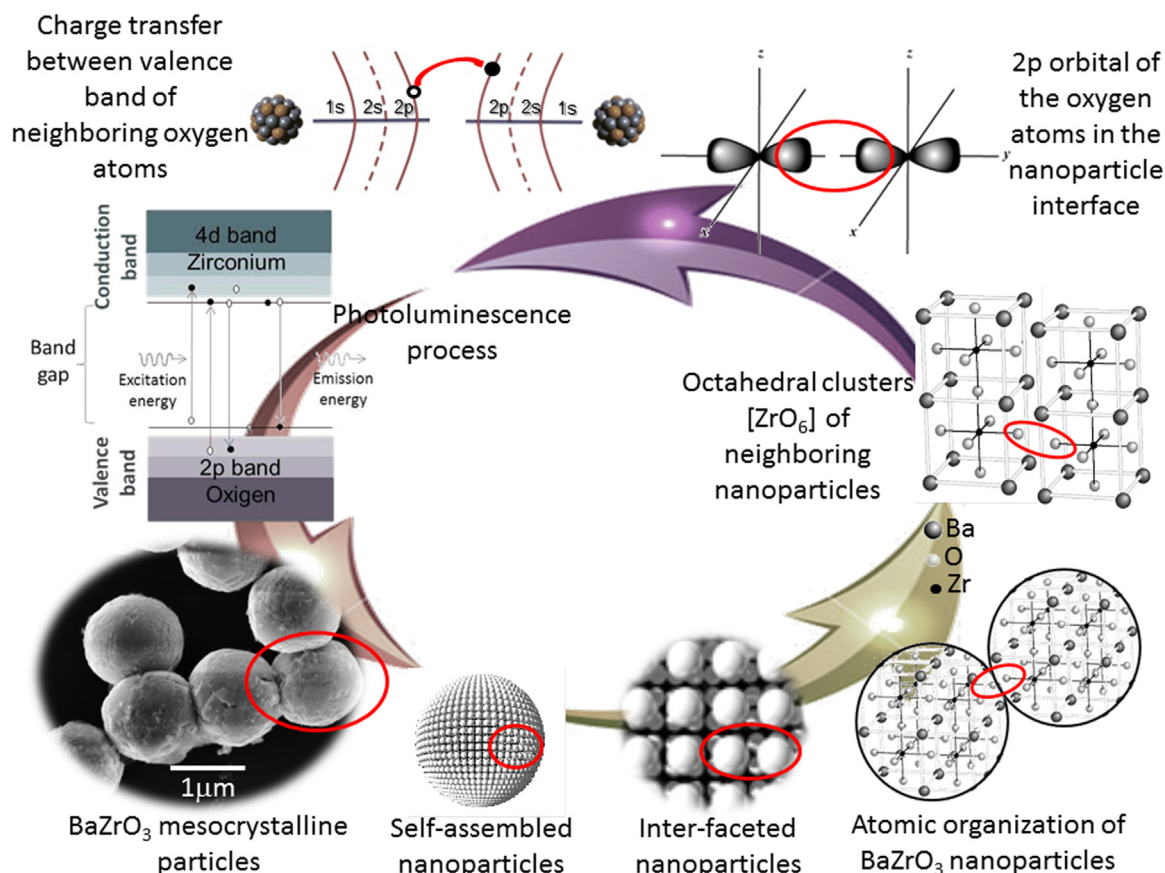


Fig. 6. Charge transfer scheme between neighboring $[\text{ZrO}_6]$ clusters.

to the profile of the PL curves. In the samples with $x=0.75$ and $x=1$, the presence of shallow defects was still observed, but there was a small shift of the peak to a higher energy region, suggesting a radiative recombination of charge carriers still closer to the VB and CB. The Zr/Ti replacement of BZT samples was responsible for the displacement of the PL curves, and this behavior agreed with the UV–vis results. The broadband photoluminescent emission is the sum of emissions from the different individual shallow (and deep) defects, which remain concomitantly in the material and differ only in the recombination of carriers (excitons) [14]. The largest PL emission intensity was observed for the BZ sample ($x=1$), showing that the high gap energy value of this sample was also associated with the presence of shallow defects, whose radiative recombination occurred between charge carriers at energy levels very near the VB and CB. This result showed that although the optical behavior of the UV–vis curve suggested a high-crystallinity material, that, in fact, agrees with the data of XRD, their photoluminescent behavior showed that the compound was not free of distortions in the lattice or defects (excitons), which are essential for an indirect transition between energy levels, producing a broadband spectrum (Fig. 5(e)). Furthermore, compounds with $x \leq 0.75$ concentration did not undergo radioactive decay, in which charge carriers (e^-) decayed between the intermediate levels near CB without light emission (phonons), while the BZ compound ($x=1$) did not undergo the same process, since it could have had a near absence of intermediate states. In the work of Cavalcante et al. [4], the BZ gap energy, determined by the polymeric precursor method, was very close (4.86 eV) to that in our work (4.93 eV). However, under excitation of 350 nm, the BZ compound described by those authors showed two emission regions (at 445 and 569 nm), where they attributed the first emission band to recombination between electrons and holes

located at shallow levels (close the VB and CB), while the second emission band was correlated with recombination in deep states, both occurring simultaneously [4]. Gupta et al. does the same observations in his work [27]. According to these authors, the BZ compound had a structure with a degree of disorder, in which complex clusters were present, favoring photoluminescent emission. In ordered structure, this photoluminescent emission disappears. Thus, for the BZ crystalline compound in our work, there still could have been clusters with local distortions, as evidenced by the Raman active modes. These distortions might have allowed a smooth shift of Zr^{4+} ions in the octahedron $[\text{ZrO}_6]$ of the lattice. This shift does not cause distortions in the crystal lattice, but can cause vacancies that act as pinning centers of electrons or holes. These vacancies may promote a cluster for cluster charge transfer and generate a higher carrier concentration, thereby giving rise to excitons that recombine and promote the photoluminescent emission. The distortion of the clusters in the BZ sample was insufficient to originate many intermediate bands in the gap, as shown the lowest energy region of the UV–vis absorption spectrum of this sample. In this case, the excitation energy (3.52 eV, 350 nm) was sufficient to cause an excess of charge carriers which concentrate very close to oxygen VB and Zr metal CB (shallow defects), whose recombination produce highest intensity of photoluminescent emission and more concentrated in the blue region of the spectrum.

Although the BZT compound shows a broadband photoluminescent emission spectrum, covering the entire visible spectrum, it is possible to observe that the PL peak emission has maximum intensity in the blue-violet region for all samples. These broadband PL spectrum is associated to the presence of intermediate energy levels to the band gap. Each corresponding wavelength emission represents a different electronic transition,

which in turn depends on the degree of structural order of each compound. It was noted, however, that adding Zr in BaTiO₃ lattice to form BZT solid solution did not cause significant changes in the emission spectrum, which is white, even for the sample with $x=1$ (ZrTiO₃).

The photoluminescent emission of BZT compound can also be associated with particle size and morphology. It was observed that photoluminescent emission intensity increased with particle growth (observed by FE-SEM images). As discussed, the BZ sample showed the highest photoluminescence intensity, whose particle size was in the micrometer range. According to XRD results, this sample had a highly ordered structure over long distances and absorption in the UV–vis region, suggesting the near absence of the intermediate band gap, also indicating a short ordering distance. However, the photoluminescent emission for this sample was more intense, which features a degree of disorder at medium distance. This result, therefore, suggests that the BZ mesocrystalline particles that are formed by self-assembly nanoparticles in an orderly process produce large crystalline particles, however, with many interfaces between them. In these interface regions, the surface of BZ nanoparticles has an excessive amount of oxygen atoms, which in turn are part of the [ZrO₆] octahedral structure of the BZ compound. In the case of nanoparticles, with a larger surface area, these clusters of complexes containing oxygen vacancies capable of trapping carriers occur excessively. Vacancies originating in the surface oxygens of the nanoparticles may thus transfer charges to surface vacancies of another oxygen ion, belonging to an adjacent cluster in a neighboring nanoparticle through the interface between them. This transfer of charges may contribute to an increase in population in oxygen VB that will be excited to Zr CB of the respective [ZrO₆] cluster, generating new electron-hole pairs, which recombine causing the photoluminescent process. Thus, BaZrO₃ micrometer mesocrystalline particles (composed of self-assembly of nanoparticles) have, in excess, defects responsible for producing photoluminescence, even in the case of a material with high structural ordering in the short and long range, as outlined in Fig. 6. In this case, there was an association between aggregate defects to disorder at medium atomic distances and the charge transfer between the interfaces of the self-assembled nanoparticles, resulting in an intense photoluminescence intensity of the BZ compound. In the case of samples with intermediate concentrations ($0.25 \leq x \leq 0.75$), the evidence of the two phases that comprise a single particle suggests that the photoluminescent emission was not influenced by the interaction between nanoparticles, i.e., there was no charge transfer between them. In these cases, the particles did not show evidence of the formation of mesocrystals from the self-assembly of nanoparticles. Here, the photoluminescent emission occurred essentially due to the intrinsic defects of each phase (characterized by UV–vis absorption tail) and not to the interface between nanoparticles via charge transfer between its neighboring clusters.

4. Conclusions

BZT compounds were prepared by the microwave-assisted hydrothermal method. The results showed that Zr/Ti isomorphic substitution improved the optical behavior of the compound, although it hindered the formation of solid solutions with long-range structural ordering. The BZ compound had special optical characteristics, compared to other samples. This compound had

high symmetry and few defects associated with the band gap, but it showed the highest associated photoluminescence. This behavior was linked to the presence of mesocrystals, formed from the self-assembly of nanoparticles, which have numerous interfaces between them. Due to this the most favorable condition for the intense photoluminescence occurs in this sample is a charge transfer between neighboring clusters in the surrounding nanoparticles interface, which causes an increase in the population responsible for the formation of excitons and consequently radioactive decay. The photoluminescence, resulting in a predominantly white color, added to BZT's high potential for application in white light-emitting devices, especially the BZ compound, which displayed the highest intensity of light.

Acknowledgements

The authors thank FAPESP/CEPID (Proc. 2013/07296-2), CNPq (573636/2008-7) and INCTMN (2008/57872-1) financing agents of this research.

References

- [1] H. Chaib, L.M. Eng, F. Schlaphof, Phys. Rev. B 71 (2005) 085418-1.
- [2] P. Seeharaj, B. Boonchom, P. Charoonsuk, P. Kim-Lohsoontorn, N. Vittayakorn, Ceram. Int. 39 (2013) S559.
- [3] L.S. Cavalcante, J.C. Sczancoski, V.M. Longo, F.S. De Vicente, J.R. Sambrano, A. T. de Figueiredo, C.J. Dalmaschio, M. Siu Li, J.A. Varela, E. Longo, Opt. Commun. 281 (2008) 3715.
- [4] L.S. Cavalcante, J.C. Sczancoski, J.W.M. Espinosa, V.R. Mastelaro, A. Michalowicz, P.S. Pizani, F.S. De Vicente, M. Siu Li, J.A. Varela, E. Longo, J. Alloy Compd. 471 (2009) 253.
- [5] E.C. Aguiar, A.Z. Simões, C.A. Paskocimas, M. Cilence, E. Longo, J.A. Varela, J. Mater. Sci. Mater. Electron 26 (2015) 1993.
- [6] M. Anicete-Santos, L.S. Cavalcante, E. Orhan, E.C. Paris, L.G.P. Simões, M.R. Joya, I.L.V. Rosa, P.R. de Lucena, M.R.M.C. Santos, L.S. Santos-Júnior, P.S. Pizani, E. R. Leite, J.A. Varela, E. Longo, Chem. Phys. 316 (2005) 206.
- [7] S.B. Reddy, K.P. Rao, M.S.R. Rao, Scr. Mater. 57 (2007) 591.
- [8] W. Cai, C. Fu, J. Gao, H. Chen, J. Alloy Compd. 480 (2009) 870.
- [9] P.A. Jha, A.K. Jha, J. Alloy Compd. 513 (2012) 580.
- [10] J.Q. Qi, X.H. Wang, H. Zhang, H. Zou, Z.B. Wang, X.W. Qi, Y. Wang, L.T. Li, H.L. W. Chan, Ceram. Int. 40 (2014) 2747.
- [11] T. Badapanda, S. Sarangi, B. Behera, S. Anwar, Curr. Appl. Phys. 14 (2014) 1192.
- [12] D.L. Wood, J. Tauc, Phys. Rev. B 5 (1972) 3144.
- [13] A.E. Souza, R.A. Silva, G.T.A. Santos, S.R. Teixeira, S.G. Antonio, M.L. Moreira, D. P. Volanti, E. Longo, Chem. Phys. Lett. 514 (2011) 301.
- [14] A.E. Souza, S.R. Teixeira, C. Morilla –Santos, W.H. Schreiner, P.N. Lisboa Filho, E. Longo, J. Mater. Chem. C 2 (2014) 7056.
- [15] L.R. Macario, M.L. Moreira, J. Andrés, E. Longo, CryEngComm 12 (2010) 3612.
- [16] M.L. Moreira, J. Andrés, V.R. Mastelaro, J.A. Varela, E. Longo, CryEngComm 13 (2011) 5818.
- [17] H. Cölfen, M. Antonietti, Mesocrystals and Nonclassical Crystallization, John Wiley & Sons, Ltd., USA, 2008.
- [18] F.C. Meldrum, H. Cölfen, Chem. Rev. 108 (2008) 4332.
- [19] A.N. Kulak, P. Iddon, Y. Li, S.P. Armes, H. Cölfen, O. Paris, R.M. Wilson, F. C. Meldrum, J. Am. Chem. Soc. 129 (2007) 3729.
- [20] W.-S. Cho, J. Phys. Chem. Solids 59 (1998) 659.
- [21] M.L. Moreira, G.P. Mambrini, D.P. Volanti, E.R. Leite, M.O. Orlandi, P.S. Pizani, V. R. Mastelaro, C.O. Paiva-Santos, E. Longo, J.A. Varela, Chem. Mater. 20 (2008) 5381.
- [22] M.-W. Chu, Y. Shingaya, T. Nakayama, Appl. Phys. A 86 (2007) 101.
- [23] G. Yang, Z. Yue, T. Sun, J. Zhao, Z. Yang, L. Li, Appl. Phys. A 91 (2008) 119.
- [24] T. Charoonsuk, W. Vittayakorn, N. Vittayakorn, P. Seeharaj, S. Maensiri, Ceram. Inter 41 (2015) S87.
- [25] L.S. Cavalcante, M. Anicete-Santos, J.C. Sczancoski, L.G.P. Simões, M.R.M. C. Santos, J.A. Varela, P.S. Pizani, E. Longo, J. Phys. Chem. Solids 69 (2008) 1782.
- [26] L.M. Schabbach, A.M. Bernardin, M.C. Fredel, Cerâm. Ind. 7 (2002) 35.
- [27] S.K. Gupta, N. Pathak, R.M. Kadam, J. Lumin. 169 (2016) 106.